Characterization of Subsynchronous Oscillation with Wind Farms Using Describing Function and Generalized Nyquist Criterion

Yanhui Xu ⓘ, *Member, IEEE*, Zheng Gu, and Kai Sun ⓘ, *Senior Member, IEEE*

Abstract—Eigen-analysis is widely used in the studies of power system oscillation and small-signal stability. However, it may give inaccurate analyses on subsynchronous oscillation (SSO) when nonlinearity is not negligible. In this paper, a nonlinear analytical approach based on the describing function and generalized Nyquist criterion is proposed to analyze the characteristics of SSO with wind farms. The paper first presents describing function-based model reduction considering key nonlinear elements involved in SSO, and then uses a generalized Nyquist criterion for accurate estimation of SSO amplitude and frequency. The results are verified by time-domain simulations on a detailed model with different scenarios considering variations of the system condition and controller parameters.

Index Terms—Wind farm, subsynchronous oscillation, describing function, generalized Nyquist criterion.

I. INTRODUCTION

SUBSYNCHRONOUS oscillation (SSO) with wind farms has become one of the main stability issues of modern power systems integrating wind generations. There have been a number of studies on SSO with wind farms in literature. For instance, ref. [1] builds a doubly-fed induction generator (DFIG) based wind farm model for SSO analysis. Ref. [2] identifies the induction generator effect as the mechanism of SSO rather than torsional interaction. Ref. [3] reports an SSO event in Texas, USA in 2009, which was caused by subsynchronous control interactions between wind turbines and line series capacitors. Ref. [4] proposes an aggregated circuit model to intuitively explain and quantitatively evaluate the SSO with DFIG-based wind farms. Ref. [5] reports an SSO event of the permanent magnet synchronous generator (PMSG)-based wind

farm that was firstly observed in Xinjiang power gird of China in 2015. Its mechanism is found that the wind farm appears as an impedance with capacitance and small negative resistance in a certain range of subsynchronous frequencies. It forms a resistance-inductance-capacitance negative-damping oscillator circuit with the AC system, which leads to SSO. Ref. [5] employs both eigen-analysis and impedance-based modeling approach to investigate the dynamic interactions between PMSGs and the AC network. Such an impedance-based modeling approach has been widely used for studying stability problems caused by grid-connected voltage source converters (VSCs) [6]- [12]. Several impedance-based stability criterions for VSCs are proposed in [13]–[15]. Paper [16] provides a state-space representation to analyze subsynchronous interactions between two different PMSGs, and the SSO characteristics under different system parameters are also discussed. In addition to eigen-analysis and impedance-based approach, papers [17]–[20] use a linearized model to derive the subsynchronous dynamic responses with the control systems of VSCs. It is pointed out that subsynchronous responses can be amplified by the feedback loop of VSCs.

Linear system analysis methods and an impedance-based approach have successfully identified some causes of the SSO with wind farms in literature. However, when nonlinearities of the system contribute to SSO, they need to be modeled and addressed appropriately for accurate estimation on SSO. Field data have shown that a DFIG or PMSG-based wind farm may have non-growing, sustained SSO when a saturation or control limit is met [3], [5]. Therefore, in order to estimate the amplitude and frequency of SSO accurately, the influence of the VSC controller saturation nonlinearity should not be ignored. Accurate estimation on SSO is important since abnormal voltage or current values in SSO can damage wind generators like the damage to the crowbar circuit in the Texas SSO event in 2009 [3]. Moreover, if the frequency of the wind farm SSO coincides with the torsional vibration frequency of the nearby thermal power unit shaft, the thermal power unit will undergo torsional vibration. For instance, the aforementioned Xinjiang wind farm SSO event in 2015 caused a thermal power unit to trip due to torsional vibrations [5].

This paper proposes a nonlinear analytical approach based on the describing function and generalized Nyquist criterion (for short, the DF-GNC approach) to characterize the SSO with a DFIG or PMSG-based wind farm. Firstly, the describing function method introduced by [21]–[23] is employed to model

the saturation nonlinearity in the VSC control systems. Then, a generalized Nyquist criterion is used to analyze the characteristic of sustained SSO and estimate its amplitude and frequency. Finally, time domain simulations with a detailed model are conducted to validate this DF-GNC approach under different scenarios like changing the power grid strength and control parameters with the phase-locked loop (PLL) and inner current control loop (CCL). Research results indicate that the DF-GNC approach can provide more accurate characteristics of the wind farm SSO than linear system analysis.

The rest of this paper is organized as follows: Section II introduces the DF-GNC approach. In Section III, the model of a PMSG-based wind farm connected to a power grid is established. The characteristics of the wind farm SSO are studied respectively by the DF-GNC approach, eigen-analysis and time domain simulations. The frequencies and amplitudes of the SSO estimated by different methods are compared. Finally, conclusions are drawn in Section IV.

II. PROPOSED APPROACH BASED ON DESCRIBING FUNCTION AND GENERALIZED NYQUIST CRITERION

The dynamic performance of a wind farm connected to a power grid can be modeled by a set of nonlinear differential and algebraic equations.

$$\dot{x} = f(x, y)$$
$$0 = g(x, y) \tag{1}$$

where $x \in R^{n_x}$ is the vector of state variables, e.g., rotor speeds and angles of wind turbine generators, rotor and stator currents, state variables of controllers, etc. and $y \in R^{n_y}$ is the vector of non-state variables, e.g., bus voltage magnitudes and angles.

To estimate the frequency and amplitude of SSO with the wind farm, a traditional approach is to linearize (1) and perform eigen-analysis or apply Nyquist criterion. However, some nonlinearities that may significantly influence oscillation characteristics such as saturation or dead-band elements will be lost. This paper proposes the following analytical approach based on DF-GNC for more accurate analysis of SSO characteristics as shown in Fig. 1.

First of all, assume that the characteristics of SSO can significantly be influenced by some critical nonlinear elements existing in some of functions of $g(x, y)$, such as saturation effects. Denote these functions by g_2 and the rest of g by g_1, i.e., rewriting (1) as:

$$\begin{cases} \dot{x} = f(x, y) \\ 0 = g_1(x, y) \end{cases} \tag{2}$$

$$0 = g_2(x, y) \tag{3}$$

Next, apply a mathematical tool named the "describing function" to analyze the characteristics of SSO caused by g_2. Meanwhile, the response of the rest of the system are modeled by a conventional transfer function, which can integrate the describing functions on nonlinear elements in g_2. Then, the frequency and amplitude of SSO can be obtained from the transfer function using generalized Nyquist criterion. The details are presented as follows.
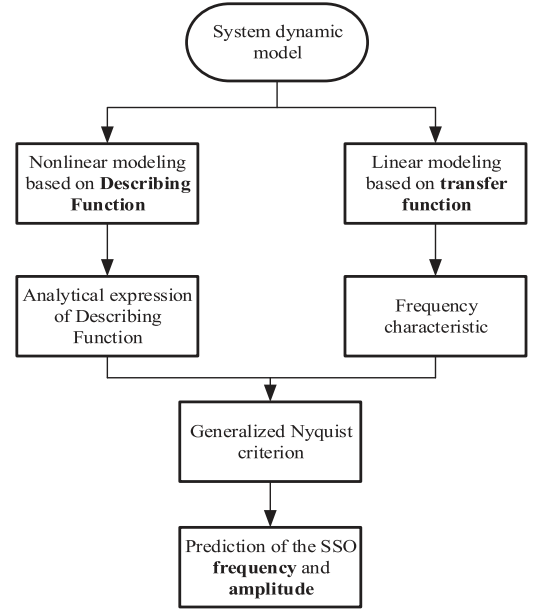

Fig. 1. Flowchart of the nonlinear analytical approach based on DF-GNC.

A. Describing Function

The describing function method was proposed in the 1940s for nonlinear control system analysis and design [21]. It is generally used to analyze stability and predict oscillation properties, such as frequency and amplitude, for nonlinear oscillator systems and has been successfully applied to oscillator design and analysis [24], [25]. It has been widely applied to the power electronics field, e.g., for calculating AC transfer characteristics of DC/DC converters [26]. Many studies and engineering practices in recent years show that the describing function method is concise and effective in analyzing stability, especially oscillatory characteristics of a control system containing nonlinear elements.

For a nonlinear element modeled by function $y = h(x)$, whose characteristics do not change with time, a sinusoidal input x does not necessarily result in a sinusoidal output y, but the output y is guaranteed to be periodical having the same frequency as the input signal. Thus, assume the input to be a sinusoidal signal with amplitude A, i.e., $x(A, t) = A\sin\omega t$, and output $y(A, t) = h(A\sin\omega t)$ can be decomposed into a Fourier series so as to obtain the coefficient at fundamental frequency $\omega/2\pi$, which is denoted by $Y(A)$ and reflects the oscillation amplitude at the fundamental frequency. A describing function is defined by (4), which describes how much the oscillation amplitude A of the input signal $x(A, t)$ is changed by the nonlinear function $h(x)$:

$$N(A) = Y(A)/A. \tag{4}$$

Considering that $Y(A)$ is complex, re-write $N(A)$ as

$$N(A) = \frac{1}{A}(a_1 + jb_1) \tag{5}$$

$$\begin{cases} a_1 = +\frac{1}{\pi}\int_0^{2\pi} h(A \cdot \sin\omega t) \cdot \sin\omega t d\omega t \\ b_1 = -\frac{1}{\pi}\int_0^{2\pi} h(A \cdot \sin\omega t) \cdot \cos\omega t d\omega t \end{cases} \tag{6}$$

Thus, each nonlinear element can be replaced by a function only depending on the oscillation amplitude A, not the angular frequency ω if $h(x)$ is a memoryless algebraic function. This nonlinear element is regarded as a variable gain amplifier that varies with the input signal amplitude.

Take the saturation characteristic function as an example:

$$h(x) = \begin{cases} -k\delta, & x \leq -\delta \\ kx, & -\delta < x < \delta \\ k\delta, & x \geq \delta \end{cases} . \qquad (7)$$

With input $x(A, t) = A \cdot \sin\omega t$, output $y(A, t)$ is

$$y(A, t) = \begin{cases} k\delta, & 2k\pi + \phi < \omega t < (2k+1)\pi - \phi \\ -k\delta, & (2k+1)\pi + \phi < \omega t \\ & < (2k+2)\pi - \phi \\ kA\sin(\omega t), & \text{everywhere else} \end{cases} \qquad (8)$$

where $k \in Z$ and $\phi = \arcsin(\delta/A)$, assuming $A \geq \delta$. There is

$$a_1 = \frac{2kA}{\pi} \left[\arcsin\left(\frac{\delta}{A}\right) + \frac{\delta}{A}\sqrt{1 - \left(\frac{\delta}{A}\right)^2} \right]. \qquad (9)$$

Similarly, we have

$$b_1 = -\frac{1}{\pi} \int_0^{2\pi} h(A \cdot \sin(\omega t)) \cos(\omega t) \, d\omega t = 0. \qquad (10)$$

Finally, the analytical expression of the describing function for saturation function can be calculated as

$$N(A) = \frac{2k}{\pi} \left[\arcsin\left(\frac{\delta}{A}\right) + \frac{\delta}{A}\sqrt{1 - \left(\frac{\delta}{A}\right)^2} \right], A \geq \delta. \qquad (11)$$

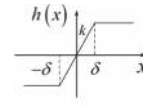The describing functions of several common nonlinearities in power systems are listed in Table I.
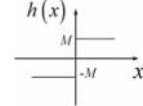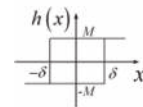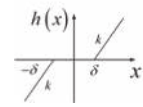
In power systems, other typical nonlinear elements are such as the dead-bands in speed governing systems, saturation elements in voltage-source converter (VSC) control systems and some controllers in photovoltaic generation whose critical nonlinear components can be modeled as ideal relay elements as shown in the second row of Table I.

Apply the describing function method to model the critical nonlinear elements in (3) and the Fourier transform to create the model in (2). Then, the system model can be obtained, so that the generalized Nyquist criterion can be used to analyze the SSO characteristics of the system.

B. Frequency and Amplitude Prediction Using Generalized Nyquist Criterion

For a single-input single-output (SISO) system, assume that its transfer function can be represented as Fig. 2, where the $R(j\omega)$ and $C(j\omega)$ are the input and output, $N(A)$ is the describing function on its nonlinear element of interest and $G(j\omega)$ contains all linear elements, or in other words, the rest of the system whose nonlinearity can be ignored such as equations in (2). The

TABLE I
DESCRIBING FUNCTIONS OF SEVERAL COMMON NONLINEARITIES

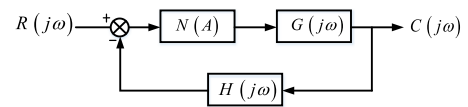| Names	Nonlinearities	Describing Functions
Saturation		$N(A) = \frac{2k}{\pi}\left[\arcsin\left(\frac{\delta}{A}\right) + \frac{\delta}{A}\sqrt{1 - \left(\frac{\delta}{A}\right)^2}\right], A \geq \delta$
Ideal Relay		$N(A) = \frac{4M}{\pi A}$
Hysteresis Relay		$N(A) = \frac{4M}{\pi A}\sqrt{1 - \left(\frac{\delta}{A}\right)^2} - j\frac{4M\delta}{\pi A^2}, A \geq \delta$
Dead-band		$N(A) = \frac{2k}{\pi}\left[\frac{\pi}{2} - \arcsin\left(\frac{\delta}{A}\right) - \frac{\delta}{A}\sqrt{1 - \left(\frac{\delta}{A}\right)^2}\right], A \geq \delta$

Fig. 2. Typical structure of a nonlinear system.

closed-loop characteristic equation of the system is

$$1 + N(A)G_0(j\omega) \qquad (12)$$

where the open-loop transfer function $G_0(j\omega) = G(j\omega)H(j\omega)$.

In the Nyquist criterion, the case where $G_0(j\omega)$ surrounds the point $(-1, j0)$ in a linear system can be extended to the case where $G_0(j\omega)$ surrounds the curve $-1/N(A)$ in a nonlinear system. This is called as the generalized Nyquist criterion. Two lemmas under this particular condition can be deduced [27]:

1) If the linear part of the nonlinear system is stable, meaning that the transfer function of the linear part has no poles on the right half plane, the necessary and sufficient condition for stability of the closed-loop system is that the Nyquist plot of $G_0(j\omega)$ does not surround the curve $-1/N(A)$.

2) If the linear part of the nonlinear system is unstable, meaning that the transfer function of the linear part has P poles on the right half plane, the necessary and sufficient condition for the stability of the closed-loop system is that the Nyquist plot of $G_0(j\omega)$ needs to surround the curve $-1/N(A)$ for P times in the counter-clockwise direction.

If $G_0(j\omega)$ does not have any poles on the right half plane under the given parameters, the necessary condition for the system to be marginally stable is

$$G_0(j\omega) = -\frac{1}{N(A)}. \qquad (13)$$

The condition (13) is satisfied only when the plot of $-1/N(A)$ on complex plane graphically intersects with the Nyquist plot
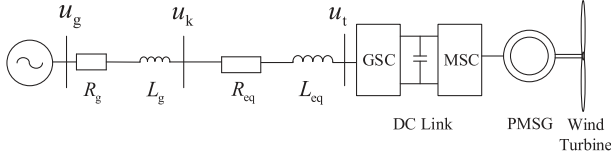
Fig. 3.   System model with PMSG-based wind farm connected to AC grid.

Fig. 4.   Block diagram of GSC.

of $G_0(j\omega)$. The ω and A at the intersection provide predictions to the oscillation's frequency and amplitude, respectively.

In fact, according to the formula (13) and the describing functions on nonlinear components, analytical formulas may be derived for direct calculation of the oscillation amplitude A. For a trivial example, considering a system involving only the ideal relay nonlinearity, the oscillation amplitude A can be calculated by $A = -\frac{4MG_0(j\omega)}{\pi}$ according to (13) and Table I.

In the following, for an oscillating system whose nonlinearity is dominated by the saturation nonlinearity in Table I, a procedure is presented for deriving an approximate formula on amplitude A:

First, let $x = \frac{\delta}{A} \in [-1, 1]$. From (11) and (13), there is

$$\arcsin x + x\sqrt{1 - x^2} = -\frac{\pi}{2kG_0(j\omega)} \qquad (14)$$

Then, replace the left hand side by its truncated Taylor series up to the 3rd order to yield:

$$x^3 - 6x - \frac{3\pi}{2kG_0(j\omega)} = 0. \qquad (15)$$

Its real root is solvable analytically and can be plugged into (16) to calculate the amplitude.

$$A = \frac{\delta}{x}. \qquad (16)$$

In the next case study section, the amplitudes estimated by this formula will be compared to more accurate results from the proposed DF-GNC approach for estimating the oscillation amplitude of SSO that is dominated by saturation nonlinearity. The following case study will demonstrate a high accuracy of this analytical formula.

III. CASE STUDY

The nonlinear analytical approach based on DF-GNC can be employed to analyze various oscillation issues in power systems. In this section, we take the SSO problem with a PMSG-based wind farm as a case to validate the effectiveness of the proposed DF-GNC approach for SSO characterization.

A. System Modeling

Fig. 3 shows a PMSG-based wind turbine generator as an equivalence of a wind farm connected to a weak AC grid. The wind farm is assumed to have N identical type-4 wind turbine generators (WTGs) of K MW each. Each generator consists of a wind turbine, a PMSG, a machine-side converter (MSC), a DC link, and a grid-side converter (GSC). The VSC bridge arm resistance and inductance are ignored in this model.
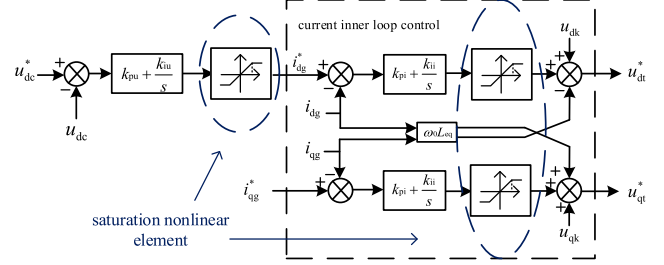
In Fig. 3, R_g and L_g are the equivalent resistance and inductance of the grid, respectively, R_{eq} and L_{eq} are the equivalent resistance and inductance of the transformer and filter, u_g is the infinite bus voltage, u_k is the point of common coupling (PCC) voltage, and u_t is the terminal voltage of the GSC. The main circuit dynamics are modeled in the x-y orthogonal reference frame, which rotates counterclockwise with synchronous angular velocity ω_0

$$\begin{cases} sL_{eq}i_{xg} = -R_{eq}i_{xg} + \omega_0 L_{eq}i_{yg} + u_{xt} - u_{xk} \\ sL_{eq}i_{yg} = -R_{eq}i_{yg} - \omega_0 L_{eq}i_{xg} + u_{yt} - u_{yk} \end{cases} \qquad (17)$$

$$\begin{cases} sL_g i_{xg} = -R_g i_{xg} + \omega_0 L_g i_{yg} + u_{xk} - u_{xg} \\ sL_g i_{yg} = -R_g i_{yg} - \omega_0 L_g i_{xg} + u_{yk} - u_{yg} \end{cases} \qquad (18)$$

where i_{xg} and i_{yg} represent the x-axis and y-axis line currents of the main circuit, u_{xt} and u_{yt} are the x-axis and y-axis terminal voltages of the GSC, u_{xk} and u_{yk} are the x-axis and y-axis PCC voltages, u_{xg} and u_{yg} are the x-axis and y-axis infinite bus voltages.

In addition to the main circuit, the most important part in wind farm is its control system which mainly consists of the PLL and the VSC control system. It is widely known that the SSO in PMSGs mainly arises from the control strategy of GSC. Therefore, this paper mainly focuses on GSC control parameters. The output of the proportional integral (PI) controller often has a hard amplitude limit, which can be modeled by a saturation element as shown in Fig. 4.

Here u_{dc} is the dc-bus capacitor voltage, i_{dg} and i_{qg} are the line currents in the d-q reference frame which are obtained from the network current using transformation of coordinates, u_{dk} and u_{qk} represent the PCC voltages, u_{dt} and u_{qt} represent the GSC voltages in the d-q reference frame, the superscript "*" indicates the reference value of each operating parameter, k_{pu} and k_{iu} are the proportional gain and integral gain of voltage outer-loop control respectively, k_{pi} and k_{ii} are the CCL proportional and integral gain respectively. After modeling the saturation nonlinear elements as shown in Fig. 4, the dynamic equations of GSC control system are

$$i^*_{dg} = G_u N_u(A)(u^*_{dc} - u_{dc})$$

$$\begin{cases} u^*_{dt} = u_{dk} + G_i N_i(A)\left(i^*_{dg} - i_{dg}\right) - \omega_0 L_{eq}i_{qg} \\ u^*_{qt} = u_{qk} + G_i N_i(A)\left(i^*_{qg} - i_{qg}\right) + \omega_0 L_{eq}i_{dg} \\ G_u = k_{pu} + k_{iu}/s \\ G_i = k_{pi} + k_{ii}/s \end{cases} \qquad (19)$$

where $N_{\mathrm{u}}(A)$ and $N_{\mathrm{i}}(A)$ are the describing functions of voltage and current control loop saturation functions.

PLL includes x-y to d-q reference frame transformation. The d-q reference frame rotates counterclockwise with synchronous angular velocity ω_0, and the relation between x-y and d-q reference frames is

$$\begin{bmatrix} f_d \\ f_q \end{bmatrix} = \begin{bmatrix} \cos\theta & \sin\theta \\ -\sin\theta & \cos\theta \end{bmatrix} \begin{bmatrix} f_x \\ f_y \end{bmatrix}. \tag{20}$$

where θ is the angle difference between the synchronous rotation angle and the output angle of PLL. f_{x} and f_{y} are the components of electrical quantity f in x-y reference frame, and f_{d}, f_{q} are the components of f in d-q reference frame. Here, f represents the current i_g and the voltages u_{t}, u_{k}, u_{g}.

The PLL model is

$$\theta_{\mathrm{p}} = \left(\frac{sk_{pp} + k_{ip}}{s} u_{\mathrm{qk}} + \omega_0 \right) / s = \theta + \omega_0 t \tag{21}$$

where k_{pp} and k_{ip} are the PLL proportional gain and integral gain respectively, θ_{p} is the output angle of PLL.

Details on the rest of the system shown in Fig. 3 can be found in [28] and [29]. Keeping all nonlinearities of the model will cause complexities in analyses and computations, so it is advisable to divide all nonlinearities into two categories: "hard" and "soft" nonlinearities. In VSCs, the "hard" ones can refer to saturation nonlinearities, and the "soft" ones are, e.g., reference transformations. Compared with "hard" nonlinearities, small-signal models that linearize "soft" nonlinearities may be used without much sacrifice on the accuracy of oscillation or resonance analysis [30]. These "hard" and "soft" nonlinearities can correspond to the "nonlinear part" and "linear part" of the system assumed by the Describing Function method.

In order to derive the transfer function on the linear part, choose the line current reference as the input and the actual value of the line current as the output. To analyze the stability of the current control loop, the DC voltage control is ignored. The q-axis current reference i_{qg}^* is zero when the constant reactive power control is employed to the system. After linearizing and simplifying (17)–(21), the current control expressions can be simplified as

$$\begin{cases} \Delta i_{xg} = \frac{KG_{\mathrm{i}}(1+N_i(A)I-N_i(A)\mathrm{J}_1)}{1+N_i(A)(I-I\cdot\mathrm{J}_1+I\cdot\mathrm{J}_2)}\Delta i_{\mathrm{dg}}^* \\ \Delta i_{yg} = \frac{(KG_{\mathrm{i}})^2\mathrm{J}_3(1+N_i(A)I)}{1+N_i(A)(I-I\cdot\mathrm{J}_1+I\cdot\mathrm{J}_2)}\Delta i_{\mathrm{dg}}^* \end{cases} \tag{22}$$

K, I and J_1 to J_3 can be calculated by these formulas:

$$\mathrm{K} = \frac{N_i\,(\mathrm{A})}{N_i\,(\mathrm{A})\,G_{\mathrm{i}} + sL_{eq} + R_{eq}} \tag{23}$$

$$I = \frac{G_{\mathrm{i}}}{sL_{eq} + R_{eq}} \tag{24}$$

$$\mathrm{J}_1 = G_{\mathrm{PLL}}\left(sL_g + R_g\right)i_{xg0} \tag{25}$$

$$\mathrm{J}_2 = G_{\mathrm{PLL}}\omega_0 L_g i_{yg0} \tag{26}$$

$$\mathrm{J}_3 = G_{\mathrm{PLL}}\omega_0 L_g i_{xg0} \tag{27}$$

$$G_{PLL} = (sk_{pp} + k_{ip})/(s^2 + sk_{pp} + k_{ip}) \tag{28}$$

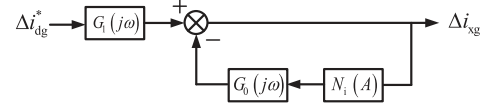Fig. 5. d/x-axis current closed-loop control block diagram.

TABLE II
MAIN PARAMETERS OF THE STUDY SYSTEM

Variable	Value	Variable	Value
Number of WTGs	800	Capacity of a WTG(MW)	1.5
R_g(p.u.)	0	$k_{\mathrm{iu}}(s^{-1})$	800
L_g(p.u.)	0.855	k_{pi}	10
R_{eq}(p.u.)	0.003	$k_{\mathrm{ii}}(s^{-1})$	40
L_{eq}(p.u.)	0.3	k_{pp}	50
k_{pu}	4	$k_{ip}(s^{-1})$	2500

Note: Base Capacity $S_{\mathrm{B}} = 1200\mathrm{MVA}$

TABLE III
TWO OTHER SETS OF PARAMETERS OF VSC

Parameters of G_0'	Value	Parameters of G_0''	Value
L_{eq}(mH)	0.15	L_{eq}(mH)	0.1
k_{pi}	0.9	k_{pi}	2
$k_{\mathrm{ii}}(s^{-1})$	50	$k_{\mathrm{ii}}(s^{-1})$	100
k_{pp}	50	k_{pp}	60
$k_{ip}(s^{-1})$	900	$k_{ip}(s^{-1})$	1400

In (25), (26) and (27), the subscript 0 represents the initial value of each operating parameter. Taking the d/x-axis current for example, its closed-loop control block diagram is shown in Fig. 5.

In Fig. 5, $G_0(j\omega)$ represents the frequency characteristics of the linear part including the "soft" nonlinear elements. The mathematical expressions of $G_0(j\omega)$ and $G_1(j\omega)$ are

$$G_0(j\omega) = I - I \cdot \mathrm{J}_1 + I \cdot \mathrm{J}_2 \tag{29}$$

$$G_1(j\omega) = KG_{\mathrm{i}}\left(1 + N_i(A)I - N_i(A)\mathrm{J}_1\right). \tag{30}$$

B. Estimation of the SSO Characteristics by the DF-GNC

Main parameters affecting the characteristic of SSO are studied to provide references of the magnitude and frequency to possible practical outcomes as shown in Table II.

Under a sinusoidal signal input, if the linear element of the system has a low-pass filtering characteristic, the amplitude of the system output at a high frequency will be much smaller than the amplitude at the fundamental frequency. Thus, the output of the nonlinear system will be much closer to its response at the fundamental frequency. Characterizing the nonlinear element with a describing function under such a condition is more accurate. We select two other sets of controller parameters in the reference [20], [31] as shown in Table III, and obtain G_0' and G_0'' respectively according to (29). The Bode diagram of $G_0(s)$ under three sets of controller parameters is shown in Fig. 6.

From Fig. 6, the amplitude-frequency and the phase-frequency plots on $G_0(\mathrm{s})$ are similar under different parameter settings, so the Bode plot of the $G_0(j\omega)$ with parameters in
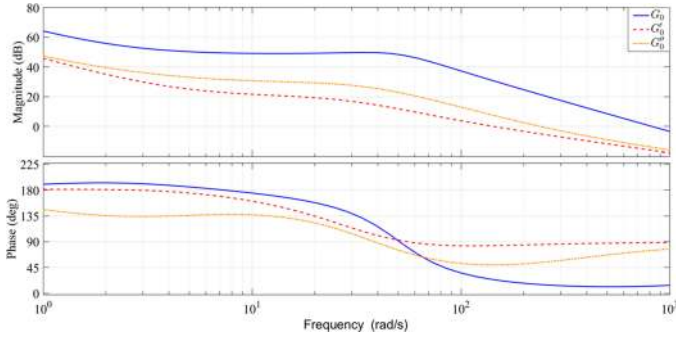
Fig. 6.   Bode plot of $G_0(j\omega)$.

(a) Nyquist plots under different L_g.

(b) Nyquist plots under different k_{pp}.

(c) Nyquist plots under different k_{ip}.

(d) Nyquist plots under different k_{pi}.

(e) Nyquist plots under different k_{ii}

Fig. 7.   Nyquist plots under different conditions.

Table II is typical of converters used in PMSGs. From the amplitude-frequency plots, the slopes are flat at low frequencies range and become steeper in the higher-frequency range. The linear parts under different parameters all have excellent low-pass filtering characteristics. Therefore, it is reasonable to use a describing function to model the nonlinear element. For the current inner-loop control, the describing function of this saturation nonlinear element is

$$N_i(A) = \frac{2}{\pi}\left[\arcsin\left(\frac{0.05}{A}\right) + \frac{0.05}{A}\sqrt{1 - \left(\frac{0.05}{A}\right)^2}\right],$$

$$A \geq 0.05. \quad (31)$$

Now, use the DF-GNC approach to characterize the wind farm SSO under different power grid strengths, PLL and CCL parameters. Based on the parameters of the base case as shown in Table II, separately change the grid inductance L_g, the PLL proportional and integral coefficients k_{pp} and k_{ip}, the CCL proportional and integral coefficients k_{pi} and k_{ii}. The Nyquist plots of $G_0(j\omega)$ under different conditions and the plot of $-1/N_i(A)$ overlaid in the same complex plane as shown in Fig. 7.

According to the result from the proposed DF-GNC approach, it can be inferred that the wind farm can have sustained SSO since the Nyquist curves intersect with the curve of $-1/N(A)$, meaning that the system is marginally stable.

Moreover, the amplitudes and frequencies of sustained SSOs with different parameters can be estimated by the DF-GNC approach as shown in Table IV.

The sign "↓" or "↑" indicate that the variable is decreasing or increasing. From Table IV, the amplitude of SSO becomes bigger with a lower grid strength (namely a larger inductance L_g), a higher PLL proportional and integral gains, a higher CCL integral gain or a lower CCL proportional gain. The frequency of SSO becomes higher with a higher grid strength or higher PLL proportional and integral gains. The frequencies are almost constant with the variations of the CCL proportional and integral gains.

According to the formulas (14)–(16) and (24)–(29), the oscillation amplitude can approximately be estimated. Table V compares the estimations with the results from the proposed DF-GNC for different L_g, which are very close.
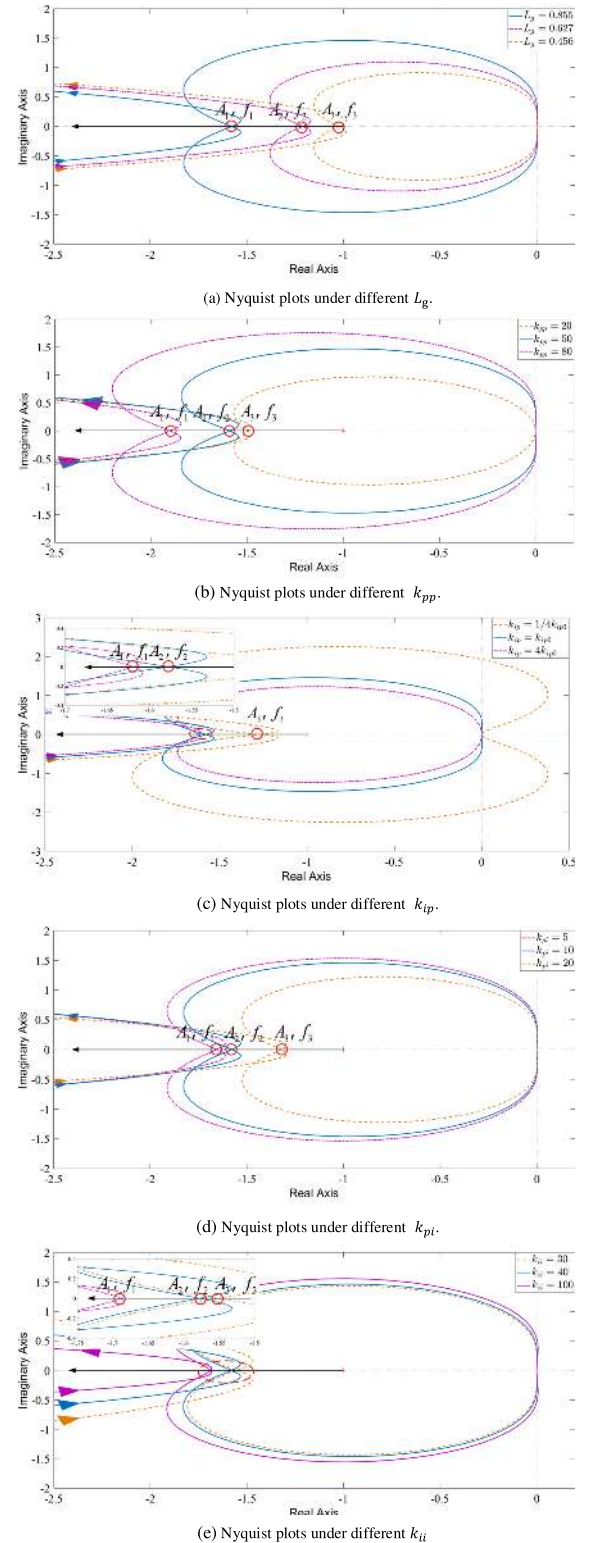
C. Comparison With Eigen-Analysis of SSO

This section provides the eigen-analysis results on the SSO as a comparison with the DF-GNC approach. A linearized model for the system in Fig. 3 can be derived in the d-q reference

TABLE IV
THE SSO AMPLITUDE AND FREQUENCY ESTIMATED BY DF-GNC

Variable	$L_g \downarrow$	$k_{pp} \downarrow$	$k_{ip} \downarrow$	$k_{pi} \uparrow$	$k_{ii} \downarrow$
A_1(p.u.)	0.0951	0.1204	0.0976	0.0991	0.1033
A_2 (p.u.)	0.0720	0.0951	0.0951	0.0951	0.0951
A_3(p.u.)	0.0546	0.0881	0.0724	0.0769	0.0939
f_1(Hz)	19.73	20.21	21.49	19.73	19.73
f_2(Hz)	20.51	19.73	19.73	19.73	19.73
f_3(Hz)	21.72	19.23	18.01	19.77	19.73

TABLE V
THE SSO AMPLITUDES ESTIMATED BY DF-GNC AND APPROXIMATED
ANALYTICAL FUNCTION WITH DIFFERENT GRID INDUCTANCE

L_g	Magnitude	DF-GNC	Approximated Analytical Function
0.855	A_1(p.u.)	0.0951	0.0953
0.627	A_2(p.u.)	0.0720	0.0726
0.456	A_3(p.u.)	0.0546	0.0572

TABLE VI
OSCILLATORY EIGENVALUES RELATED TO VSC AND AC GRID

Mode	Eigenvalues	Frequency
$\lambda_{1,2}$(p.u.)	$-46 \pm j689.22 \times 2\pi$	689.22 Hz
λ_3(p.u.)	-452.36	0 Hz
λ_4(p.u.)	-88.71	0 Hz
$\boldsymbol{\lambda_{5,6}}$**(p.u.)**	$\boldsymbol{1.81 \pm j19.67 \times 2\pi}$	**19.67 Hz**
$\lambda_{7,8}$(p.u.)	$-10.50 \pm 10.50 \times 2\pi$	2.62 Hz

TABLE VII
PARTICIPATION FACTORS OF STATE VARIABLES

State Variable	Participation Factor
x_1	0.0303
x_2	**0.2317**
x_3	0.0018
x_4	**0.1415**
i_{dg}	**0.1656**
i_{qg}	0.0021
θ_p	**0.3117**
u_{dc}	**0.1153**

frame as

$$\Delta \dot{\boldsymbol{X}} = \boldsymbol{A}\Delta\boldsymbol{X} + \boldsymbol{B}\Delta\boldsymbol{U}$$

$$\Delta\boldsymbol{X} = [\Delta x_1 \ \Delta x_2 \ \Delta x_3 \ \Delta x_4 \ \Delta i_{dg} \ \Delta i_{qg} \ \Delta\theta_p \ \Delta u_{dc}] \quad (32)$$

where $\Delta\boldsymbol{X}$ and $\Delta\boldsymbol{U}$ are incremental state vector and control vector, respectively. $\boldsymbol{A}$ and $\boldsymbol{B}$ are coefficient matrices. x_1 is the intermediate state variable of voltage outer control loop in GSC; x_2 and x_3 are the intermediate state variables of current inner control loop in GSC; x_4 is the intermediate state variable of PLL. θ_p is the output angle of PLL. The eigenvalues that are closely related to the GSC and AC grid are listed in Table VI.

Obviously, there exist a pair of conjugate eigenvalues with frequency located in the SSO frequency range. For the unstable SSO mode, participation factors of state variables are shown in Table VII.
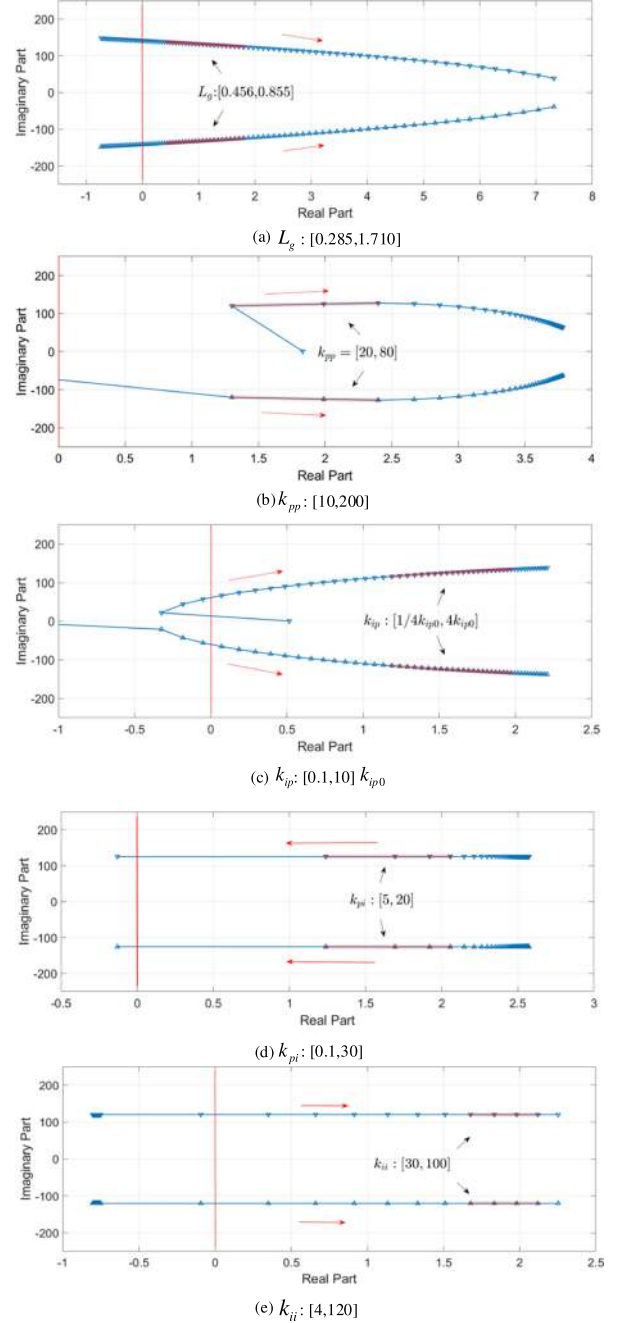

(a) L_g : [0.285,1.710]

(b) k_{pp}: [10,200]

(c) k_{ip}: [0.1,10] k_{ip0}

(d) k_{pi}: [0.1,30]

(e) k_{ii}: [4,120]

Fig. 8. The SSO mode varies with parameters.

Clearly, there are some highly participating variables, e.g., x_2, x_4, i_{dg}, θ_p, and u_{dc}. In addition to the PLL parameters, the other parameters such as k_{pi} and k_{ii} in current control would also influence the system stability. The change of the small-signal stability regarding the SSO mode with different parameters is illustrated in Fig. 8.

Fig. 8 depicts how the eigenvalues related to the SSO mode change with different parameters. As L_g or k_{ii} increases, the eigenvalues move toward the right, meaning degeneration of stability with the increase of weakness in grid connection and k_{ii}. As k_{pp} or k_{ip} increases, the eigenvalues will move toward the

TABLE VIII
THE REAL PART AND FREQUENCY OF THE SSO EIGENVALUE

Variable	$L_g \downarrow$	$k_{ip} \downarrow$	$k_{ip} \downarrow$	$k_{pi} \uparrow$	$k_{ii} \downarrow$
σ_1	1.81	2.33	1.96	2.06	2.14
σ_2	1.16	1.81	1.81	1.81	1.81
σ_3	0.44	1.36	1.19	1.25	1.66
f_1(Hz)	19.67	20.13	21.44	19.67	19.68
f_2(Hz)	20.6	19.67	19.67	19.69	19.67
f_3(Hz)	21.82	19.18	17.91	19.7	19.67
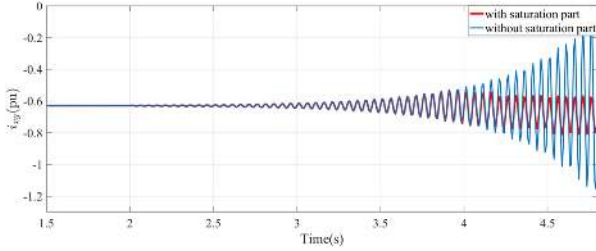
(a) Dynamics of the current i_{xg}.
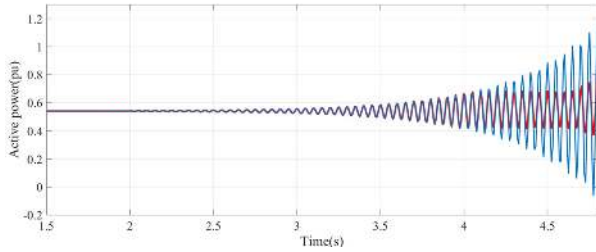
(b) Dynamics of the active power.

Fig. 9. Dynamics of PMSG-based wind farm with or without nonlinearity saturation.

left and then the right significantly. However, when k_{pi} grows, the real part of the eigenvalues will decrease to cross the imaginary axis at the critical parameter level. Table VIII lists the real parts (σ_1, σ_2, σ_3) and frequencies (f_1, f_2, f_3) of certain SSO eigenvalues which are printed in red in Fig. 8.

Based on the base case shown in Table II, when L_g is equal to 0.855, 0.627 and 0.456, respectively, the real parts and frequencies are shown in the second column. Similarly, the columns 3 to 6 show the results when k_{pp} is 80, 50 and 20, k_{ip} is $4k_{ip0}$, k_{ip0} and $1/4k_{ip0}$, k_{pi} is 5, 10, and 20, k_{ii} is 100, 40, and 30, respectively. It shows that the real parts of the eigenvalues are all positive. Through eigen-analysis, we can only get the conclusion that the system is unstable, which means the growing SSO will occur rather than the sustained SSO.

D. Nonlinear Time-Domain Simulations

The time-domain simulations are performed using Matlab Simulink, and the basic parameter settings as shown in Table II. The dynamics of SSO with and without the saturation nonlinearity following a step change of line reactance are investigated. The base-case scenario is used, and the reactance is initially set as 0.285 pu. Then, it is suddenly raised to 0.855 pu at 2 s, which weakens the connection to the AC grid. The curves of the active power and the current i_{xg} from 1.5 s to 4.8 s are shown in Fig. 9. The SSO current or active power both exponentially diverge when there is no saturation nonlinearity, which is consistent
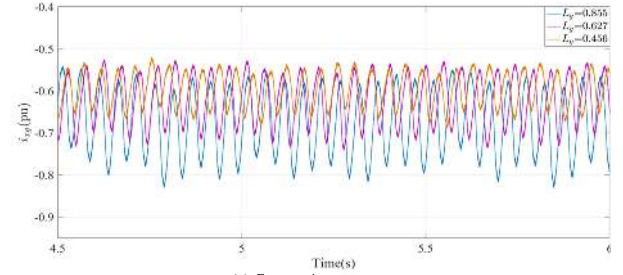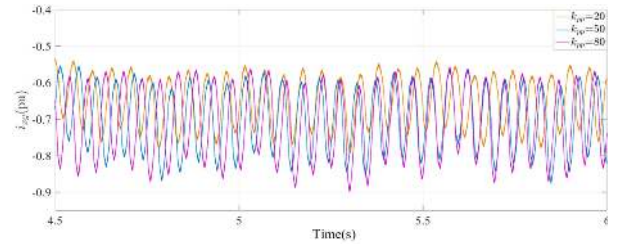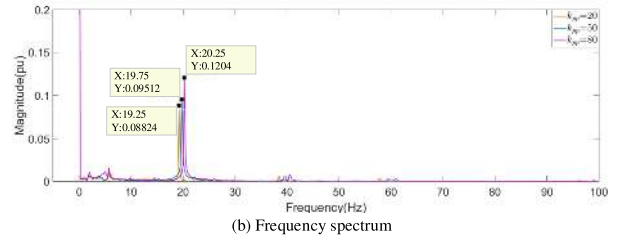

(a) Current i_{xg} response
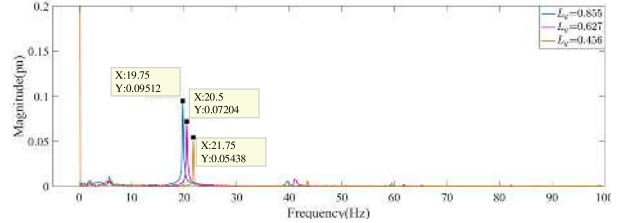
(b) Frequency spectrum

Fig. 10. Current i_{xg} response and frequency spectrum under different L_g.

(a) Current i_{xg} response

(b) Frequency spectrum

Fig. 11. Current i_{xg} response and frequency spectrum under different k_{pp}.

with the unstable SSO mode 5,6 as predicted by eigen-analysis in Table VI. When the saturation nonlinearity exists, the SSO current or active power demonstrate sustained oscillation as they reach the hard limit. Fig. 9 to Fig. 14 present the effect of the grid inductance L_g, the PLL proportional and integral coefficients k_{pp} and k_{ip}, and the CCL proportional and integral coefficient k_{pi} and k_{ii} on the sustained SSO characteristics. The variation extent of parameters are the same as the DF-GNC and eigen-analysis.

From Fig. 9 to Fig. 14, the wind farm demonstrates sustained oscillations, whose amplitudes and frequencies are shown in Table IX.

From Table IV and Table IX, the simulation results match well the results from the DF-GNC approach. To clarify the difference between the eigen-analysis and the DF-GNC approach, select some of the results from Table IV, Table VIII and Table IX and compare them in Table X and Table XII.
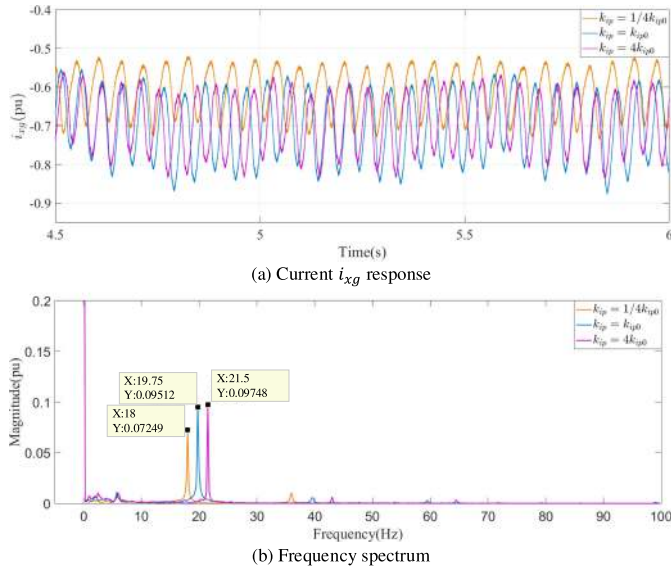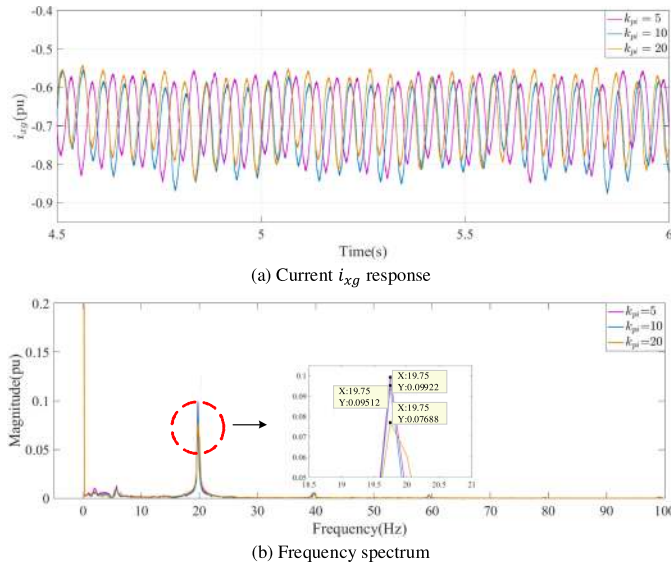
(a) Current i_{xg} response

(b) Frequency spectrum

Fig. 12.   Current i_{xg} response and frequency spectrum under different k_{ip}.

(a) Current i_{xg} response

(b) Frequency spectrum

Fig. 14.   Current i_{xg} response and frequency spectrum under different k_{ii}.

(a) Current i_{xg} response

(b) Frequency spectrum

Fig. 13.   Current i_{xg} response and frequency spectrum under different k_{pi}.

TABLE IX
THE SSO AMPLITUDE AND FREQUENCY BY SIMULATION

Variable	$L_g \downarrow$	$k_{pp} \downarrow$	$k_{ip} \downarrow$	$k_{pi} \uparrow$	$k_{ii} \downarrow$
A_1(p.u.)	0.0951	0.1204	0.0975	0.0992	0.1034
A_2 (p.u.)	0.0720	0.0951	0.0951	0.0951	0.0951
A_3(p.u.)	0.0544	0.0882	0.0725	0.0769	0.0941
f_1(Hz)	19.75	20.25	21.50	19.75	19.75
f_2(Hz)	20.50	19.75	19.75	19.75	19.75
f_3(Hz)	21.75	19.25	18.00	19.75	19.75

TABLE X
THE FREQUENCY OF SSO BY DIFFERENT METHODS

Case	Simulation Frequency (Hz)	Eigen-anlysis Frequency (Hz)	DF-GNC Frequency (Hz)	E_E (%)	E_N (%)
Base case	19.75	19.67	19.73	0.41	0.10
Case 1	21.75	21.82	21.72	0.32	0.14
Case 2	19.25	19.18	19.23	0.36	0.10
Case 3	18.00	17.91	18.01	0.5	0.06
Case 4	19.75	19.7	19.77	0.25	0.10
Case 5	19.75	19.67	19.73	0.41	0.10

Note: Case 1, $L_g = 0.456$; Case 2, $k_{pp} = 20$; Case 3, $k_{ip} = 1/4$ k_{ip0}; Case 4, $k_{pi} = 20$; Case 5, $k_{ii} = 30$.

TABLE XI
THE FREQUENCY OF SSO BY DIFFERENT METHODS

Case	Simulation Frequency (Hz)	Eigen-anlysis Frequency (Hz)	DF-GNC Frequency (Hz)	E_E (%)	E_N (%)
k_{pp}=110	20.5	20.01	20.49	1.17	0.05
k_{pp}=120	20.5	19.97	20.53	2.59	0.15
k_{pp}=130	20.75	19.85	20.71	4.34	0.19

Table X lists the oscillation frequencies under 6 cases using the three different methods. The base case is shown in Table II. The rest of the cases in the first column is obtained by changing one of the parameters in Table II. The second to fourth columns are frequencies by simulation, eigen-analysis and DF-GNC, respectively. Taking the simulation results as the references, E_E and E_N are errors of the eigen-analysis and the DF-GNC respectively. From Table X, errors from both methods are less than 1%, and the eigen-analysis has a slightly bigger error. When k_{pp} is increased to 110, 120, and 130, the error of the eigen-analysis also increases as shown by Table XI while the DF-GNC still gives accurate estimates on frequency.

Similarly, the oscillation magnitudes are listed in Table XII, which shows that the results from DF-GNC are very close to the
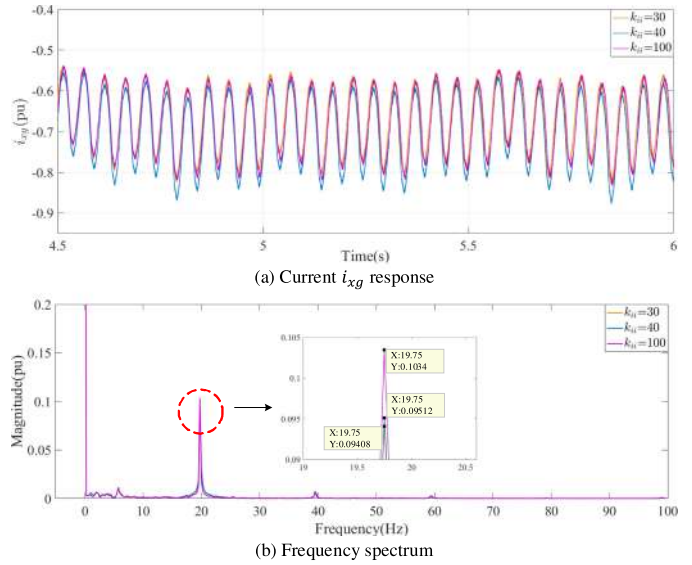
TABLE XII
THE MAGNITUDE OF SSO BY DIFFERENT METHODS

Case	Simulation Magnitude (pu)	Eigen-analysis Magnitude (pu)	DF-GNC Magnitude (pu)	E_E (%)	E_N (%)
Base case	0.0951	-	0.0951	-	0
Case 1	0.0544	-	0.0546	-	0.36
Case 2	0.0882	-	0.0881	-	0.11
Case 3	0.0725	-	0.0724	-	0.13
Case 4	0.0769	-	0.0769	-	0
Case 5	0.0941	-	0.0939	-	0.21

Note: Case 1, $L_g = 0.456$; Case 2, $k_{pp} = 20$; Case 3, $k_{ip} = 1/4\ k_{ip0}$; Case 4, $k_{pi} = 20$; Case 5, $k_{ii} = 30$.

(a) Current i_{xg} response
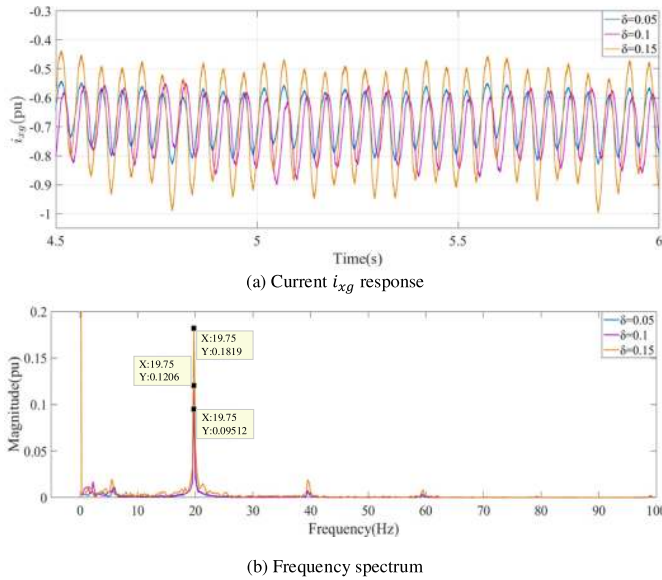
(b) Frequency spectrum

Fig. 15. X-axis current response and frequency spectrum under different limit values of the saturation nonlinearity.
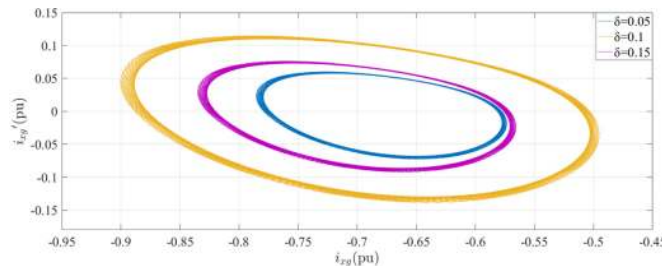

Fig. 16. X-axis current phase diagrams of i_{xg} under different limit values of the saturation nonlinearity.

simulation results. Therefore, eigen-analysis can only be used to obtain the oscillation frequency and stability of the system. However, the DF-GNC used in this paper can calculate the oscillation frequency and amplitude, and it has advantages in the accuracy and completeness of the SSO characteristic.

Fig. 15 and Fig. 16 present the current response and phase diagrams under different limit values of the saturation nonlinearity. We can see that the amplitude will increase with the more

considerable limit value of the saturation nonlinearity. Under the effect of saturation nonlinearity, the trajectory of the current phasor eventually approaches a limit cycle, and the bigger the limit value is, the larger the limit cycle reaches.

IV. CONCLUSION

The DF-GNC based approach is proposed to characterize the SSO with wind farms. The research results of a PMSG-based wind farm connected to a power gird indicate that the DF-GNC approach can predict the sustained SSO characteristics and the estimated SSO amplitudes are close to those of time domain simulation with a detailed model. The SSO frequencies estimated by the DF-GNC approach are more accurate than the results from conventional eigen-analysis. The cases with different grid strengths, PLL proportional and integral gains, CCL proportional and integral gains have validated the feasibility and correctness of the proposed DF-GNC approach for characterization of the SSO with wind farms.

REFERENCES

[1] A. Ostadi, A. Yazdani, and R. K. Varma, "Modeling and stability analysis of a DFIG-based wind-power generator interfaced with a series-compensated line," *IEEE Trans. Power Del.*, vol. 24, no. 3, pp. 1504–1514, Jul. 2009.

[2] L. Fan, R. Kavasseri, Z. L. Miao, and C. Zhu, "Modeling of DFIG-based wind farms for SSR analysis," *IEEE Trans. Power Delivery*, vol. 25, no. 4, pp. 2073–2082, Oct. 2010.

[3] G. D. Irwin, A. K. Jindal, and A. L. Isaacs, "Sub-synchronous control interactions between type 3 wind turbines and series compensated AC transmission systems," in *Proc. Power Energy Soc. General Meeting*, 2011, pp. 1–6.

[4] H. K. Liu, X. Xie, C. Zhang, Y. Li, H. Liu, and Y. Hu, "Quantitative SSR analysis of series-compensated DFIG-based wind farms using aggregated RLC circuit model," *IEEE Trans. Power Syst.*, vol. 32, no. 1, pp. 474–483, Jan. 2017.

[5] H. Liu, X. Xie, J. He, X. Tao, Y. Zhao, and W. Chao, "Subsynchronous interaction between direct drive PMSG based wind farms and weak AC networks," *IEEE Trans. Power Syst.*, vol. 32, no. 6, pp. 4708–4720, Nov. 2017.

[6] X. Wang, L. Harnefors, and F. Blaabjerg, "Unified impedance model of grid connected voltage-source converters," *IEEE Trans. Power Electron.*, vol. 33, no. 2, pp. 1775–1787, Feb. 2018.

[7] L. Harnefors, M. Bongiorno, and S. Lundberg, "Input-admittance calculation and shaping for controlled voltage-source converters," *IEEE Trans. Ind. Electron.*, vol. 54, no. 6, pp. 3323–3334, Dec. 2007.

[8] B. Wen, D. Dong, D. Boroyevich, R. Burgos, P. Mattavelli, and Z. Shen, "Impedance-based analysis of grid-synchronization stability for three phase paralleled converters," *IEEE Trans. Power Electron.*, vol. 31, no. 1, pp. 26–38, Jan. 2016.

[9] B. Wen, D. Boroyevich, R. Burgos, P. Mattavelli, and Z. Shen, "Analysis of D-Q small-signal impedance of grid-tied inverters," *IEEE Trans. Power Electron.*, vol. 31, no. 1, pp. 675–687, Jan. 2016.

[10] K. Alawasa, Y. A.-R. I. Mohamed, and W. Xu, "Modeling, analysis, and suppression of the impact of full-scale wind-power converters on subsynchronous damping," *IEEE Syst. J.*, vol. 7, no. 4, pp. 700–712, Dec. 2013.

[11] M. Cespedes and J. Sun, "Impedance modeling and analysis of grid-connected voltage-source converters," *IEEE Trans. Power Electron.*, vol. 29, no. 3, pp. 1254–1261, Mar. 2014.

[12] A. Rygg, M. Molinas, C. Zhang, and X. Cai, "A modified sequence-domain impedance definition and its equivalence to the dq-domain impedance definition for the stability analysis of AC power electronic systems," *IEEE J. Emerg. Sel. Topics Power Electron.*, vol. 4, no. 4, pp. 1383–1396, Dec. 2016.

[13] J. Sun, "Impedance-based stability criterion for grid-connected inverters," *IEEE Trans. Power Electron.*, vol. 26, no. 11, pp. 3075–3078, Nov. 2011.

[14] H. Liu, X. Xie, and W. Liu, "An oscillation stability criterion based on the unified dq-Frame impedance network model for power systems with high-penetration renewables," *IEEE Trans. Power Syst.*, vol. 33, no. 3, pp. 3472–3485, May 2018.

[15] W. Du, X. Chen, and H. Wang, "Power system electromechanical oscillation modes as affected by dynamic interactions from grid-connected PMSGs for wind power generation," *IEEE Trans. Sustain. Energy*, vol. 8, no. 3, pp. 1301–1312, Jul. 2017.

[16] B. Huang, H. Sun, Y. Liu, L. Wang, and Y. Chen, "Study on subsynchronous oscillation in D-PMSGs-based wind farm integrated to power system," *IET Renewable Power Gener.*, vol. 13, no. 1, pp. 16–26, 2019.

[17] Y. Xu and Y. Cao, "Sub-synchronous oscillation in PMSGs based wind farms caused by amplification effect of GSC controller and PLL to harmonics," *IET Renewable Power Gener.*, vol. 12, no. 7, pp. 844–850, 2018.

[18] Y. Xu, S. Zhao, Y. Cao, and K. Sun, "Understanding subsynchronous oscillations in DFIG-based wind farms without series compensation," *IEEE Access*, vol. 7, pp. 107201–107210, 2019.

[19] Y. Xu and S. Zhao, "Mitigation of subsynchronous resonance in series-compensated DFIG wind farm using active disturbance rejection control," *IEEE Access*, vol. 7, pp. 68812–68822, 2019.

[20] T. Bi, J. Li, P. Zhang, E. Mitchell-Colgan, and S. Xiao, "Study on response characteristics of grid-side converter controller of PMSG to sub-synchronous frequency component," *IET Renewable Power Gener.*, vol. 11, no. 7, pp. 966–972, 2017.

[21] R. J. Kochenburger, "A frequency response method for analyzing and synthesizing contactor servomechanisms," *Transactions of the American Institute of Electrical Engineers*, vol. 69, no. 1, pp. 270–284, 1950.

[22] A. Gelb and W. Vander Velde, *Multiple-Input Describing Functions and Nonlinear System Design*. New York, USA: McGraw-Hill, 1968.

[23] H. K. Khalil, "The describing function method," in *Nonlinear Systems*, 3th ed. New Jersey, USA: Prentice-Hall, 1996, pp.450–468

[24] J. Bank, *A Harmonic-oscillator Design Methodology based on Describing Functions*. Chalmers University of Technology, 2006.

[25] E. Vidal, A. Poveda, and M. Ismail, "Describing functions and oscillators," *IEEE Circuits Devices Mag.*, vol. 17, no. 6, pp. 7–11, Nov. 2001.

[26] H. S. H. Chung, A. Ionovici, and J. Zhang, "Describing functions of power electronics circuits using progressive analysis of circuit waveforms," *IEEE Trans. Circuits Syst. I: Fundamental Theory Appl.*, vol. 47, no. 7, pp. 1026–1037, Jul. 2000.

[27] W. Zhang, and Z. Yang, "Stability analysis of nonlinear systems with non-minimum phase," *Control Instruments Chemical Industry (in Chinese)*, vol. 14, no. 1, pp. 12–14, 1986.

[28] K. M. Alawasa, Y. A. I. Mohamed, and W. Xu, "Modeling, analysis, and suppression of the impact of full-scale wind-power converters on subsynchronous damping," *IEEE Syst. J.*, vol. 7, no. 4, pp. 700–712, Dec. 2013.

[29] K. M. Alawasa, Y. A. I. Mohamed, and W. Xu, "Active mitigation of subsynchronous interactions between PWM voltage-source converters and power networks," *IEEE Trans. Power Electron.*, vol. 29, no. 1, pp. 121–134, Jan. 2014.

[30] S. Shah and L. Parsa, "Large-signal impedance for the analysis of sustained resonance in grid-connected converters," in *Proc. IEEE 18th Workshop Control Modeling Power Electron. (COMPEL)*, 2017, pp. 1–8.

[31] Y. Huang, X. Yuan, J. Hu, and P. Zhou, "Modeling of VSC connected to weak grid for stability analysis of DC-link voltage control," *IEEE J. Emerg. Sel. Topics Power Electron.*, vol. 3, no. 4, pp. 1193–1204, Dec. 2015.

Yanhui Xu (M'07) received the B.S., M.S., and Ph.D. degrees from North China Electric Power University, Beijing, China, in 2001, 2004, and 2010, respectively.

He is currently an Associate Professor with the School of Electrical and Electronic Engineering, North China Electric Power University. His research interests include power system sub-synchronous oscillation, low-frequency oscillation, and load modeling.

Zheng Gu was born in Heibei province, China, in 1995. She received the B.S. degree in electrical engineering and automation from North China Electric Power University, Beijing, China, in 2017, and the Postgraduate degree with the School of Electrical and Electronic Engineering, North China Electric Power University, in 2017.

Her research interests include power system stability and integration of wind power.
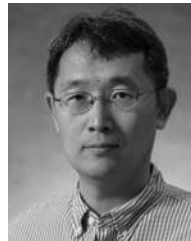
Kai Sun (M'06–SM'13) received the B.S. degree in automation and the Ph.D. degree in control science and engineering from Tsinghua University, Beijing, China, in 1999 and 2004, respectively. He is currently an Associate Professor with the Department of EECS, University of Tennessee, Knoxville, TN, USA. He was a Project Manager in grid operations and planning with the EPRI, Palo Alto, CA, USA, from 2007 to 2012. He is an Editor for the IEEE TRANSACTIONS ON POWER SYSTEMS, IEEE TRANSACTIONS ON SMART GRID, IEEE ACCESS, and IEEE OPEN ACCESS JOURNAL OF POWER AND ENERGY.